

# Robust Tube-based Control Strategy for Vision-guided Autonomous Vehicles

Der-Hau Lee

**Abstract**—A robust control strategy for autonomous vehicles can improve system stability, enhance riding comfort, and prevent driving accidents. This paper presents a novel interpolation tube-based constrained iterative linear quadratic regulator (itube-CILQR) algorithm for autonomous computer-vision-based vehicle lane-keeping. The goal of the algorithm is to enhance robustness during high-speed cornering on tight turns. The advantages of itube-CILQR over the standard tube-approach include reduced system conservatism and increased computational speed. Numerical and vision-based experiments were conducted to examine the feasibility of the proposed algorithm. The proposed itube-CILQR algorithm is better suited to vehicle lane-keeping than variational CILQR-based methods and model predictive control (MPC) approaches using a classical interior-point solver. Specifically, in evaluation experiments, itube-CILQR achieved an average runtime of 3.16 ms to generate a control signal to guide a self-driving vehicle; itube-MPC typically required a 4.67-times longer computation time to complete the same task. Moreover, the influence of conservatism on system behavior was investigated by exploring the interpolation variable trajectories derived from the proposed itube-CILQR algorithm during lane-keeping maneuvers.

**Index Terms**—Autonomous vehicles, constrained iterative linear quadratic regulator, tube model predictive control, deep neural networks.

## I. INTRODUCTION

A Control law for a given dynamical system must often be identified in many scientific, engineering and real-world tasks. With developments in computing, optimization-based model predictive control (MPC) techniques have widely attracted interest from practitioners to guide working systems. MPC methods can optimize forecasts of a constrained system behavior over a finite time horizon window based on a state-space model with an associated performance-based cost function. An MPC controller generates a control law, which is a solution to the associated regulation problem in the case of optimal control. MPC controllers are more flexible than classic linear quadratic regulator (LQR) controllers for solving complicated control problems with various constraints. For these problems, LQR often cannot provide an analytic solution. MPC algorithms can also be used in feedback control by solving the open-loop optimal control problem repeatedly. The resulting state feedback law can then be used as the manipulable inputs for regulating a system [1], [2]. However, the forecasting quality of a classical MPC algorithm can be degraded in the presence of uncertainty, oversimplification, mistaken model assumptions, or external disturbances to the

state or control variables. To enhance the robustness of classical MPC, researchers have proposed tube-based MPC approaches [3]. Tube-MPC requires all trajectories of the system to lie in a bounded neighborhood (a tube) that satisfies the system constraints. The cross-section of the tube is determined by introducing uncertainty to a suitably constrained nominal (noise-free) system. To avoid generating an excessively large tube, a feedback control policy  $u$  is applied to actual system where  $u = \bar{u} + K(x - \bar{x})$  and  $\bar{x}$  and  $\bar{u}$  are the nominal state and control variables, respectively. The LQR feedback gain  $K$  is selected to regulate the deviation between the actual and nominal states such that this deviation converges to zero. Tube-MPC methods ensure robustness, stability, and constraint fulfillment and have therefore been widely used in recent automotive [4], [5], [6], [7], [8] and robotics [9], [10], [11], [12], [13] applications.

In [4], the authors developed a force-input nonlinear bicycle model and applied it in a tube-MPC controller to maneuver a vehicle for a static obstacle avoidance task. In several trials of the controlled system under random external noise, they showed that the vehicle trajectories produced by the tube-MPC controller were much tighter (i.e., less scattered) than those of a classical MPC controller. In [5], the authors investigated a vehicle lane-keeping application based on a linear single-track model. Tube-MPC was used to ensure ride comfort and driving stability if model deviations occurred. In [6], the authors proposed a unified framework for a self-driving vehicle which was navigated by a tube-MPC controller to robustly and safely follow a reference trajectory which was generated by a Frenet frame planner. The vehicle could also avoid dynamic obstacles. The control part of the framework accounted for not only the external state and control disturbances but also internal model uncertainty. Online estimation of the size of state disturbance was achieved through Gaussian process regression. In [7], a tube-MPC control strategy was proposed and applied to achieve path-following for four-wheel independent drive automated vehicles. This model had time-varying uncertainty attributable to tire cornering stiffness. However, the control performance of conservative (restrictive) tube-MPC was worse than that of classical MPC when white noise was added to the state variables. In [8], the authors proposed a stochastic tube-MPC method subjected to constraints with probability distributions. A dynamic feedback gain mechanism was designed by leveraging covariance steering theory, and the tightened constraints were determined by applying the concept of probabilistic reachable sets. The nominal constraint region was larger for stochastic tube-MPC than for tube-MPC, indicating that the stochastic approach was an improvement on the excessively conservative tube-MPC method.

The author was a part of the Department of Electrophysics, National Yang Ming Chiao Tung University, Hsinchu 300, Taiwan. e-mail: der-haulee@gmail.com.

In [9], trajectory tracking for a mobile robot with longitudinal slip was solved using the tube-MPC technique. The investigated system was decomposed into time-invariant and time-varying parts, and a specific set of control gains was selected to compensate for the corresponding system dynamics such that the mismatch between the actual and the nominal systems approached zero. Instead of using fixed feedback gains in tube-MPC, the authors in [10] proposed the online fusion of multiple tubes determined by different control gains by using an interpolation method. This counteracted mismatches between prediction and reality. This approach guaranteed robust stability, feasible trajectories, and constraint satisfaction at a marginal increase in computational cost. Moreover, it has a larger range of feasible region variables compared with the those in the offline approach with fixed constraint bounds. In [11] and [12], feedback from a real-world system was considered to improve tube-MPC. In the tube-MPC, an idealized nominal state is simulated forward without receiving any environmental response. Thus, the algorithm is completely reliant on the tracking ability of the feedback law for control of the system. The authors in [11] suggested using the both the actual state and nominal state as inputs to the nominal controller and comparing the resulting solutions. The superior solution was then selected as the control law for guiding the system. In [12], the authors proposed an algorithmic framework for model predictive path integral control that uses a tube-MPC technique that is a relaxed version of the mechanism in [11]. The algorithm overcame the inherent problem of low robustness in sampling-based MPC. In [13], based on the alternating direction method of multipliers algorithm, the authors introduced a rapid scaled-symmetric optimization algorithm to enhance the computational efficiency of embedded tube-MPC in a high-order unmanned aerial vehicle (UAV) system. The proposed methodology solved the trajectory tracking problem for a tiltrotor UAV carrying a suspended load.

Motivated by these works, this paper proposes an itube-CILQR control strategy based on tube-based approaches and the constrained iterative linear quadratic regulator (CILQR) algorithm [14], [15]. CILQR is a version of MPC algorithm for solving optimal control problems. The method uses barrier functions to handle system constraints in the framework of ILQR [16], [17]. These constraints are then included in the control objective to convert the original problem to an effectively unconstrained problem. This barrier-function-based strategy achieves fast computation during optimization and enables the generation of smooth solution trajectories. However, robustness is not guaranteed for the classical CILQR algorithm when applied to systems in the presence of disturbances. Therefore, we adapted several tube-MPC techniques presented in [3], [10], [11] to enhance CILQR's robustness in this study. The features of the proposed algorithm are as follows: i) Tightened constraints are computed using an outer-bounding tube with varying disturbance bounds [3]. ii) A synthesized control law capable of receiving feedback from the environment is proposed to maneuver the actual system [11]. iii) An interpolation approach that incorporates interpolation variables into the CILQR optimization procedure is used to fuse multiple tubes and to generate less conservative

tightened constraints [10]. Reducing conservatism is important because conservatism often degrades controller performance in standard tube-based approaches. To demonstrate its feasibility, this study used the proposed itube-CILQR control algorithm to solve the optimal control problem for a vehicle lane-keeping task.

Handling road curvature is key challenge in vehicle lane-keeping control. Technically, the standard single-track dynamics model becomes nonlinear when a curvature term is included [18], [19]. Solving this problem therefore requires computationally expensive nonlinear optimization, which is unsuitable for the real-time demands of many applications. Therefore, we do not solve the nonlinear lane-keeping control problem directly as was the case in previous works [19], [20]; instead, we treat the curvature term as an external disturbance source and then apply itube-CILQR to robustly solve the corresponding control problem. In our previous work [21], we proposed an efficient vision-based system that uses individual front facing camera images to perceive a vehicle's surrounding environment. The functionality of the system encompasses ego-vehicle heading angle prediction and ego-lane boundary inference. Validation in The Open Racing Car Simulator (TORCS) [22] indicated the promising performance of the system. This platform, including its visual perception system and the TORCS environment, enables real-time simulated control of vehicles by vision-guided lane-keeping algorithms. Specifically, the contributions of this study are as follows.

- 1) This study proposes a novel itube-CILQR controller based on CILQR and tube-based techniques that guarantees the robustness and stability of real-time lane-keeping control for automotive systems on large-curvature roads.
- 2) This study validated the performance of the itube-CILQR algorithm in numerical simulations and vision-based autonomous driving experiments in the realistic TORCS simulator.

The remainder of the paper is organized as follows. The adopted lane-keeping dynamics model is introduced in Section II. The MPC schemes for the lane-keeping problem are described in Section III. The proposed itube-CILQR algorithm is presented in Section IV. The experimental results and a discussion are provided in Section V. Finally, the conclusions are presented in Section VI.

## II. LANE-KEEPING DYNAMICS MODEL

This study used a bicycle model to develop a representation of vehicle lane-keeping dynamics [18]. The corresponding lateral control model is defined in terms of the distance of the ego-vehicle from the lane centerline ( $\Delta$ ), the orientation error of the ego-vehicle with respect to the road direction ( $\theta$ ), and the derivatives  $\dot{\Delta}$  and  $\dot{\theta}$  of each of these terms. For a controller designed to guide the vehicle system for automatic lane-keeping, the vehicle speed in the longitudinal direction is denoted as  $v_x$ , the front wheel steering angle is denoted as  $\delta$ , and the road curvature is denoted as  $\kappa$ . Assuming that the tire lateral force is proportional to its slip angle, the discrete-time

dynamics model for the vehicle lane-keeping control design can be written as [19], [23]

$$\mathbf{x}_{i+1} \equiv \mathbf{f}(\mathbf{x}_i, \mathbf{u}_i) = \mathbf{A}\mathbf{x}_i + \mathbf{B}\mathbf{u}_i + \mathbf{w}_i, \quad (1)$$

where the state vector and control input are defined as  $\mathbf{x} = [x_0 \ x_1 \ x_2 \ x_3]^T \equiv [\Delta \ \dot{\Delta} \ \theta \ \dot{\theta}]^T$  and  $\mathbf{u} \equiv [\delta]$ , respectively. The term  $\mathbf{w}$  containing  $\kappa$  is regarded as an external additive disturbance. The model matrices  $\mathbf{A}$ ,  $\mathbf{B}$ , and  $\mathbf{w}$  have the following form:

$$\mathbf{A} = \begin{bmatrix} a_{11} & a_{12} & 0 & 0 \\ 0 & a_{22} & a_{23} & a_{24} \\ 0 & 0 & a_{33} & a_{34} \\ 0 & a_{42} & a_{43} & a_{44} \end{bmatrix}, \quad \mathbf{B} = \begin{bmatrix} 0 \\ b_1 \\ 0 \\ b_2 \end{bmatrix}, \quad \mathbf{w} = \kappa \begin{bmatrix} 0 \\ c_1 \\ 0 \\ c_2 \end{bmatrix}$$

with the corresponding matrix coefficients:

$$\begin{aligned} a_{11} &= a_{33} = 1, & a_{12} &= a_{34} = dt, \\ a_{22} &= 1 - \frac{(2C_{\alpha f} + 2C_{\alpha r})dt}{mv_x}, & a_{23} &= \frac{(2C_{\alpha f} + 2C_{\alpha r})dt}{mv_x}, \\ a_{24} &= -\frac{(2l_f C_{\alpha f} - 2l_r C_{\alpha r})dt}{mv_x}, & a_{42} &= -\frac{(2l_f C_{\alpha f} - 2l_r C_{\alpha r})dt}{I_z v_x}, \\ a_{43} &= \frac{(2l_f C_{\alpha f} - 2l_r C_{\alpha r})dt}{I_z}, & a_{44} &= 1 - \frac{(2l_f^2 C_{\alpha f} + 2l_r^2 C_{\alpha r})dt}{I_z v_x}, \\ b_1 &= \frac{2C_{\alpha f} dt}{m}, & b_2 &= \frac{2l_f C_{\alpha f} dt}{I_z}, \\ c_1 &= -\frac{(2l_f C_{\alpha f} - 2l_r C_{\alpha r})dt}{m} - v_x^2 dt, \\ c_2 &= -\frac{(2l_f^2 C_{\alpha f} + 2l_r^2 C_{\alpha r})dt}{I_z}. \end{aligned}$$

Here,  $dt$  is the sample time;  $m$  is the vehicle mass  $I_z$  is the moment of inertia along the vertical direction;  $C_{\alpha f}$  and  $C_{\alpha r}$  are the cornering stiffness values of the front and rear tires, respectively; and  $l_f$  and  $l_r$  are the distances from the center of gravity of the vehicle to the front and rear tires, respectively. The parameters selected for the model and vehicle are listed in Table I.

As described in Sec. I, nearly optimal control inputs can be straightforwardly obtained by solving the constrained lane-keeping dynamics model (1) using the standard MPC scheme [19]. However, this strategy may be too computationally demanding in practice due to the nonlinearity of the lane curvature  $\kappa$ , compromising driving safety under extreme driving conditions, such as high speed cornering.

The objective of this study is to develop a rapid and robust tube-based controller for real-time automotive lane-keeping. To this end, (1) is first defined as the "actual" system, which is subject to constraints  $\mathbf{x} \in \mathbb{X}$ ,  $\mathbf{u} \in \mathbb{U}$ , and  $\mathbf{w} \in \mathbb{W}$  containing the origin. We assume that  $\mathbb{X}$  is closed and  $\mathbb{U}$  and  $\mathbb{W}$  are compact. In geometric terms,  $\mathbb{X}$ ,  $\mathbb{U}$ , and  $\mathbb{W}$  are polytopes. Correspondingly, the disturbance-free "nominal" system is defined by

$$\bar{\mathbf{x}}_{i+1} \equiv \bar{\mathbf{f}}(\bar{\mathbf{x}}_i, \bar{\mathbf{u}}_i) = \mathbf{A}\bar{\mathbf{x}}_i + \mathbf{B}\bar{\mathbf{u}}_i, \quad (2)$$

where  $\bar{\mathbf{x}}$  and  $\bar{\mathbf{u}}$  are the associated nominal state and control vectors, respectively. Instead of solving the constrained optimization problem for the nonlinear model in (1), one can solve this problem using the linear model in (2) and handle

TABLE I  
VALUES OF THE MODEL AND VEHICLE PARAMETERS USED IN THIS STUDY

$dt$	0.01 s	$C_{\alpha f}$	80000 N/rad
$v_x$	{20.0, 22.2} m/s	$C_{\alpha r}$	80000 N/rad
$I_z$	2000 kgm <sup>2</sup>	$l_f$	1.27 m
$m$	1150 kg	$l_r$	1.37 m

the  $\mathbf{w}$  term with a tube-based approach at a far lower computational cost for an acceptable decrease in performance. Related MPC schemes for the considered lane-keeping problem are discussed in the following sections.

### III. MPC SCHEMES FOR LANE-KEEPING PROBLEM

In this section, MPC schemes used to solve the lane-keeping problem are introduced. The details of computing tightened constraints for tube-based approaches are provided in the last part of this section.

#### A. Nominal-MPC scheme

This section details the nominal-MPC algorithm. Here, the term "nominal-MPC" refers to MPC computation using the nominal system model (2) with no consideration of robustness. The optimization variables in this control problem are a sequence of states  $\mathbf{X} \equiv \{\mathbf{x}_0, \mathbf{x}_1, \dots, \mathbf{x}_N\}$  and a control sequence  $\mathbf{U} \equiv \{\mathbf{u}_0, \mathbf{u}_1, \dots, \mathbf{u}_{N-1}\}$ . The associated optimization problem subject to constraints  $\mathbb{X}$  and  $\mathbb{U}$  is formulated as follows (Problem 1):

*Problem 1:*

$$\min_{\mathbf{X}, \mathbf{U}} J = J_s + J_t, \quad (3a)$$

$$J_s = \sum_{i=0}^{N-1} \mathbf{x}_i^T \mathbf{Q} \mathbf{x}_i + \mathbf{u}_i^T \mathbf{R} \mathbf{u}_i, \quad (3b)$$

$$J_t = \mathbf{x}_N^T \mathbf{P} \mathbf{x}_N \quad (3c)$$

subject to

$$\mathbf{x}_{i+1} = \bar{\mathbf{f}}(\mathbf{x}_i, \mathbf{u}_i), \quad 0 \leq i < N, \quad (4a)$$

$$\mathbf{x} \in \mathbb{X}, \quad (4b)$$

$$\mathbf{u} \in \mathbb{U}, \quad (4c)$$

where the total cost  $J$  comprises the stage and terminal cost functions  $J_s$  and  $J_t$ , respectively;  $N$  denotes the prediction horizon. The weighting matrices  $\mathbf{Q}$  and  $\mathbf{R}$  are assumed to be symmetric positive-definite matrices. The matrix  $\mathbf{P}$  in  $J_t$  is the solution of the discrete-time algebraic Riccati equation, which is expressed as follows:

$$\mathbf{P} = \mathbf{A}^T \mathbf{P} \mathbf{A} + \mathbf{Q} - \mathbf{A}^T \mathbf{P} \mathbf{B} (\mathbf{B}^T \mathbf{P} \mathbf{B} + \mathbf{R})^{-1} \mathbf{B}^T \mathbf{P} \mathbf{A}. \quad (5)$$

The control parameters and constraints used in (3) and (4) are listed in Table II.

The first component of the optimal control sequence of this MPC problem is chosen to guide the ego-car. The control law is

$$u = u_d \equiv u_0^*(\mathbf{x}_0), \quad (6)$$

TABLE II  
CONTROL PARAMETER VALUES AND CONSTRAINTS

$N$	30	$\mathbf{Q}$	diag[20, 1, 20, 1]
$\Delta$	[-2.0, 2.0] m	$\mathbf{R}$	60I
$\dot{\Delta}$	[-8.0, 8.0] m/s	$\mathbf{S}$	50I
$\theta$	$[-\pi/2, \pi/2]$ rad	$(q_{s1}, q_{s2})$	(5, 1)
$\dot{\theta}$	[-4.0, 4.0] rad/s	$(q_{u1}, q_{u2})$	(80, 1)
$\delta$	$[-\pi/6, \pi/6]$ rad	$(q_{l1}, q_{l2})$	(80, 1)
$\kappa$	[-0.1, 0.1] 1/m	$(q_{l3}, q_{l4})$	(20, 20)

where  $\mathbf{x}_0$  are the current actual states. Clearly, the solution to Problem 1 obtained by the nominal model (2) is a rudimentary approximation of the true solution of the MPC problem for the actual system model (1). This nominal-MPC scheme is valid for at low speed or for small-curvature roads. In our previous study [21], vehicles guided by this nominal-MPC algorithm were demonstrated to sometimes leave the lane unintentionally when entering tight turns at high speed.

### B. Tube-MPC scheme

The key concept of tube-MPC is that if the nominal state  $\bar{\mathbf{X}} \equiv \{\bar{\mathbf{x}}_0, \bar{\mathbf{x}}_1, \dots, \bar{\mathbf{x}}_N\}$  and control  $\bar{\mathbf{U}} \equiv \{\bar{\mathbf{u}}_0, \bar{\mathbf{u}}_1, \dots, \bar{\mathbf{u}}_N\}$  sequences satisfy the tightened constraints  $\bar{\mathbf{X}}$  and  $\bar{\mathbf{U}}$ , respectively, the state and control trajectories  $\mathbf{X}$  and  $\mathbf{U}$  of the actual system under a disturbance  $\mathbf{w} \in \mathbb{W}$  also satisfy the original constraints  $\mathbf{X}$  and  $\mathbf{U}$ . That is, all trajectories of the actual system lie in the tube of the tube-MPC framework. This guarantees system stability and enhances system robustness [3]. Constraint tightening is achieved by bounding the deviation of the actual state from the nominal state by using uncertainty sets  $\mathbb{S} = \mathbb{S}(\mathbb{W})$ ; the relevant computations are presented in Sec. III-D. The corresponding tube-MPC problem subject to tightened constraints is formulated as follows (Problem 2):

Problem 2:

$$\min_{\bar{\mathbf{X}}, \bar{\mathbf{U}}} \bar{J} = \bar{J}_s + \bar{J}_t, \quad (7a)$$

$$\bar{J}_s = \sum_{i=0}^{N-1} \bar{\mathbf{x}}_i^T \mathbf{Q} \bar{\mathbf{x}}_i + \bar{\mathbf{u}}_i^T \mathbf{R} \bar{\mathbf{u}}_i, \quad (7b)$$

$$\bar{J}_t = \bar{\mathbf{x}}_N^T \mathbf{P} \bar{\mathbf{x}}_N \quad (7c)$$

subject to

$$\bar{\mathbf{x}}_{i+1} = \bar{\mathbf{f}}(\bar{\mathbf{x}}_i, \bar{\mathbf{u}}_i), \quad 0 \leq i < N, \quad (8a)$$

$$\bar{\mathbf{x}} \in \bar{\mathbf{X}}, \quad (8b)$$

$$\bar{\mathbf{u}} \in \bar{\mathbf{U}}. \quad (8c)$$

The control law  $u$  for the actual system has two terms: i) the solution  $\bar{u}_{MPC}$  of the above MPC problem and ii) a tracking controller  $\bar{u}_{LQR} = \mathbf{K}(\mathbf{x} - \bar{\mathbf{x}})$  that compensates for the discrepancies between nominal and actual states, where the stabilizing LQR gain

$$\mathbf{K} = -(\mathbf{B}^T \mathbf{P} \mathbf{B} + \mathbf{R})^{-1} \mathbf{B}^T \mathbf{P} \mathbf{A} \quad (9)$$

is chosen to attenuate disturbances.

To make the nominal trajectory respond to changes in the environment, [11] compared two copies of the controller

against each other, one obtained from the nominal state ( $u_n$ ) and one obtained from the actual state ( $u_a$ ), namely

$$\begin{aligned} u_n &\equiv u(\bar{\mathbf{x}}_0) = \bar{u}_{MPC}(\bar{\mathbf{x}}_0) + \bar{u}_{LQR}(\bar{\mathbf{x}}_0) \\ &= \bar{u}_{MPC}(\bar{\mathbf{x}}_0) + \mathbf{K}(\mathbf{x}_0 - \bar{\mathbf{x}}_0) \end{aligned} \quad (10)$$

and

$$\begin{aligned} u_a &\equiv u(\mathbf{x}_0) = \bar{u}_{MPC}(\mathbf{x}_0) + \bar{u}_{LQR}(\mathbf{x}_0) \\ &= \bar{u}_{MPC}(\mathbf{x}_0), \end{aligned} \quad (11)$$

where  $\bar{\mathbf{x}}_0$  is the current nominal state and  $\bar{u}_{LQR}(\mathbf{x}_0) = 0$ . The solution with lower cost is selected as the superior and applied to control the actual system. In this study, we synthesize (10) and (11) to control the actual system. The proposed control policy ( $u_p$ ) is represented as

$$\begin{aligned} u_p &= u_n + u_a \\ &= \bar{u}_{MPC}(\bar{\mathbf{x}}_0) + \mathbf{K}(\mathbf{x}_0 - \bar{\mathbf{x}}_0) + \bar{u}_{MPC}(\mathbf{x}_0). \end{aligned} \quad (12)$$

As will be shown in Sec. V-A, the actual state trajectory can be made to converge to the target points more effectively using this joint scheme than using  $u_n$  or  $u_a$  alone. The difference between the control laws  $u_a$  (11) and  $u_d$  (6) lies in the constraints used in MPC (tightened and original constraints, respectively).

In practice, the tightened constraints  $\bar{\mathbf{X}}$  and  $\bar{\mathbf{U}}$  used in tube-MPC can be estimated offline using predefined disturbance bounds. However, tube-MPC methods with fixed uncertainty bounds often produce excessively conservative solution trajectories because worst-case disturbances do not always occur during maneuvers. To reduce conservatism and improve system performance, one can adaptively estimate  $\bar{\mathbf{X}}$  and  $\bar{\mathbf{U}}$  online by detecting the variable disturbance  $\mathbf{w}$ . For example, the road curvature  $\kappa$  is assumed to be detectable online in this study. Thus,  $\mathbf{w}$  and the corresponding tightened constraints (denoted as  $\bar{\mathbf{X}}_{det}/\bar{\mathbf{U}}_{det}$ ) can then be estimated.

### C. Interpolation Tube-MPC scheme

The online estimations of  $\bar{\mathbf{X}}_{det}$  and  $\bar{\mathbf{U}}_{det}$  are less conservative than the offline constraints  $\bar{\mathbf{X}}$  and  $\bar{\mathbf{U}}$ . However,  $\bar{\mathbf{X}}_{det}$  and  $\bar{\mathbf{U}}_{det}$  fluctuate, potentially resulting in unstable control inputs and system instability. To overcome this problem, we applied interpolation [10] to smooth the estimated tightened constraints.

Assume that the current detected road curvature is  $\kappa_{det}$  and the corresponding tightened constraints are  $\bar{\mathbf{X}}_{det} := \{\bar{x} | |\bar{x}| \leq \bar{x}_{det}\}$  and  $\bar{\mathbf{U}}_{det} := \{\bar{u} | |\bar{u}| \leq \bar{u}_{det}\}$ . In this study, we propose using looser ( $\bar{\mathbf{X}}_b/\bar{\mathbf{U}}_b$ ) and tighter ( $\bar{\mathbf{X}}_s/\bar{\mathbf{U}}_s$ ) constraints to improve the original tightened constraints ( $\bar{\mathbf{X}}_{det}/\bar{\mathbf{U}}_{det}$ ) by using interpolation techniques. The related constraint bounds are designed to satisfy the following relations:

$$0 \leq \bar{x}_s < \bar{x}_{det} < \bar{x}_b, \quad (13a)$$

$$0 \leq \bar{u}_s < \bar{u}_{det} < \bar{u}_b, \quad (13b)$$

$$\frac{\bar{x}_{det} - \bar{x}_s}{\bar{x}_{det}} = \frac{\bar{x}_b - \bar{x}_{det}}{\bar{x}_{det}} \equiv \Delta \bar{x}, \quad (13c)$$

$$\frac{\bar{u}_{det} - \bar{u}_s}{\bar{u}_{det}} = \frac{\bar{u}_b - \bar{u}_{det}}{\bar{u}_{det}} \equiv \Delta \bar{u}. \quad (13d)$$

The actual system constraint bounds are not exceeded by  $\bar{x}_b$  and  $\bar{u}_b$  here. In this study, the parameter  $\Delta\bar{x} = \Delta\bar{u} = 0.25$ . To fuse these constraints ( $\bar{\mathbf{X}}_{det}/\bar{\mathbf{U}}_{det}$ ,  $\bar{\mathbf{X}}_b/\bar{\mathbf{U}}_b$ , and  $\bar{\mathbf{X}}_s/\bar{\mathbf{U}}_s$ ), an interpolation variable sequence  $\mathbf{L} \equiv \{\Lambda_0, \Lambda_1, \dots, \Lambda_N\}$  and  $\Lambda \equiv [\lambda_s \ \lambda_d \ \lambda_b]^T$  is introduced into the optimization problem. The improved tightened constraints  $\bar{\mathbf{X}}_{int}$  and  $\bar{\mathbf{U}}_{int}$  are then calculated as follows.

$$\bar{\mathbf{X}}_{int} = \lambda_s \bar{\mathbf{X}}_s \oplus \lambda_d \bar{\mathbf{X}}_{det} \oplus \lambda_b \bar{\mathbf{X}}_b, \quad (14a)$$

$$\bar{\mathbf{U}}_{int} = \lambda_s \bar{\mathbf{U}}_s \oplus \lambda_d \bar{\mathbf{U}}_{det} \oplus \lambda_b \bar{\mathbf{U}}_b. \quad (14b)$$

Here, the symbol  $\oplus$  indicates the Minkowski sum operation for two sets. The MPC problem subject to the aforementioned interpolation tightened constraints (14) is referred to as the interpolation tube-MPC problem, which is written as follows (Problem 3):

*Problem 3:*

$$\min_{\bar{\mathbf{x}}, \bar{\mathbf{u}}, \mathbf{L}} \bar{J}_{int} = \bar{J}_s + \bar{J}_t + J_l, \quad (15a)$$

$$\bar{J}_s = \sum_{i=0}^{N-1} \bar{\mathbf{x}}_i^T \mathbf{Q} \bar{\mathbf{x}}_i + \bar{\mathbf{u}}_i^T \mathbf{R} \bar{\mathbf{u}}_i, \quad (15b)$$

$$\bar{J}_t = \bar{\mathbf{x}}_N^T \mathbf{P} \bar{\mathbf{x}}_N, \quad (15c)$$

$$J_l = \sum_{i=0}^N \Lambda_i^T \mathbf{S} \Lambda_i \quad (15d)$$

subject to

$$\bar{\mathbf{x}}_{i+1} = \bar{\mathbf{f}}(\bar{\mathbf{x}}_i, \bar{\mathbf{u}}_i), \quad 0 \leq i < N, \quad (16a)$$

$$\bar{\mathbf{x}} \in \bar{\mathbf{X}}_{int}, \quad (16b)$$

$$\bar{\mathbf{u}} \in \bar{\mathbf{U}}_{int}. \quad (16c)$$

$$\lambda_s, \lambda_d, \lambda_b > 0, \quad (16d)$$

$$\lambda_s + \lambda_d + \lambda_b = 1.0. \quad (16e)$$

Here, the quadratic term  $J_l$  (15d) with the weighting matrix  $\mathbf{S}$  is leveraged to penalize deviations from zero for the interpolation variables; the term  $J_l$  (15d) and the constraints (16d) and (16e) drive the interpolation variables to small positive numbers. To improve controller real-time performance, the tightened constraint calculation (14) could be performed offline, and the results could be stored in a look-up table for online use.

#### D. Computation of tightened constraints

For tube-based approaches, tightened constraint calculation requires the use of set algebra; however, this is computationally expensive even for a four-dimensional system [6] because the calculation involves many polytope vertices. A solution to this problem is to project the original high-dimensional system onto low-dimensional subsystems [6], [7]. In the discretized lane-keeping model (1), the disturbance term  $\mathbf{w}$  mainly involves two state variables,  $\dot{\Delta}$  and  $\dot{\theta}$ . Thus, we approximate the tightened constraint computation for the original four-dimensional system  $\mathbf{x}$  by considering the two-dimensional subsystem  $\mathbf{x}' \equiv [\dot{\Delta} \ \dot{\theta}]^T \in \mathbb{X}'$  with control

vector  $\mathbf{u}' \equiv [\delta] \in \mathbb{U}'$  and the disturbance  $\mathbf{w}' \in \mathbb{W}'$ . The relevant discrete-time dynamics model is represented as follows [24]:

$$\mathbf{x}'_{i+1} = \mathbf{A}' \mathbf{x}'_i + \mathbf{B}' \mathbf{u}'_i + \mathbf{w}', \quad (17)$$

where the model matrices are

$$\mathbf{A}' = \begin{bmatrix} a_{22} & a_{24} - v_x dt \\ a_{42} & a_{44} \end{bmatrix}, \quad \mathbf{B}' = \begin{bmatrix} b_1 \\ b_2 \end{bmatrix}, \quad \mathbf{w}' = \kappa \begin{bmatrix} c_1 \\ c_2 \end{bmatrix}.$$

The LQR gain  $\mathbf{K}' \equiv [\mathbf{K}'_0 \ \mathbf{K}'_1]$  for this subsystem is computed using the parameters listed in Table I.

We computed the tightened constraints using an outer-bounding tube of the disturbance invariant set [3]. Because  $\mathbf{A}'_{K'} \equiv \mathbf{A}' + \mathbf{B}' \mathbf{K}'$  is stable, the uncertainty sets can be defined by

$$\mathbb{S}_i \equiv \sum_{j=0}^{i-1} \mathbf{A}'_{K'}^j \mathbb{W}'. \quad (18)$$

There exists a finite integer  $N$  and a scalar  $\alpha \in [0, 1)$  that satisfies  $\mathbf{A}'_{K'}^N \mathbb{W}' \subseteq \alpha \mathbb{W}'$  and  $\mathbf{K}' \mathbf{A}'_{K'}^N \mathbb{W}' \subseteq \alpha \mathbf{K}' \mathbb{W}'$ . It follows that

$$\mathbb{S}_\infty \subseteq \frac{1}{1-\alpha} \mathbb{S}_N, \quad (19)$$

where  $\mathbb{S}_N/1-\alpha$  is a robust positively invariant (RPI) set, denoted as  $\mathbb{S}_{RPI}$ . Because  $\mathbb{W}'$  is box-constrained, it is sufficient to check only its vertices  $\mathbf{w}'_v \equiv [\pm w_{v0} \ \pm w_{v1}]^T$  to compute  $\alpha$  using the following formula [3]:

$$\alpha = \max \left( \frac{\|\mathbf{A}'_{K'}^N \mathbf{w}'_v\|_\infty}{\|\mathbf{w}'_v\|_\infty}, \frac{\|\mathbf{K}' \mathbf{A}'_{K'}^N \mathbf{w}'_v\|_\infty}{\|\mathbf{K}' \mathbf{w}'_v\|_\infty} \right). \quad (20)$$

Alternatively,  $\alpha$  can be derived by solving the following linear programming problem:

$$\max_{i=0}^{n_r-1} \left( \max_{\mathbf{z}} \alpha_i = \mathbf{F}_i \mathbf{A}'_{K'}^N \mathbf{z} \right) \quad (21)$$

subject to

$$\mathbf{F} \mathbf{z} \leq \mathbf{1}, \quad (22)$$

where  $\mathbf{z} \equiv [z_0 \ z_1]^T$  and

$$\mathbf{F} \equiv \begin{pmatrix} \frac{-1}{w_{p0}} & 0 \\ \frac{1}{w_{v0}} & 0 \\ 0 & \frac{-1}{w_{p1}} \\ 0 & \frac{1}{w_{v1}} \\ -K'_0 & -K'_1 \\ \frac{(K'_0 w_{v0} + K'_1 w_{v1})}{K'_0} & \frac{(K'_0 w_{v0} + K'_1 w_{v1})}{K'_1} \\ \frac{(K'_0 w_{v0} + K'_1 w_{v1})}{K'_0} & \frac{(K'_0 w_{v0} + K'_1 w_{v1})}{K'_1} \end{pmatrix}.$$

The values of  $n_r$  in (21) are the row numbers of the matrix  $\mathbf{F}$ . Consequently, the tightened constraints can be computed as

$$\bar{\mathbf{X}}' = \mathbb{X}' \ominus \mathbb{S}_{RPI}, \quad (23a)$$

$$\bar{\mathbf{U}}' = \mathbb{U}' \ominus \mathbf{K}' \mathbb{S}_{RPI}. \quad (23b)$$

Here, the operator  $\ominus$  defines the Pontryagin difference operation between sets.

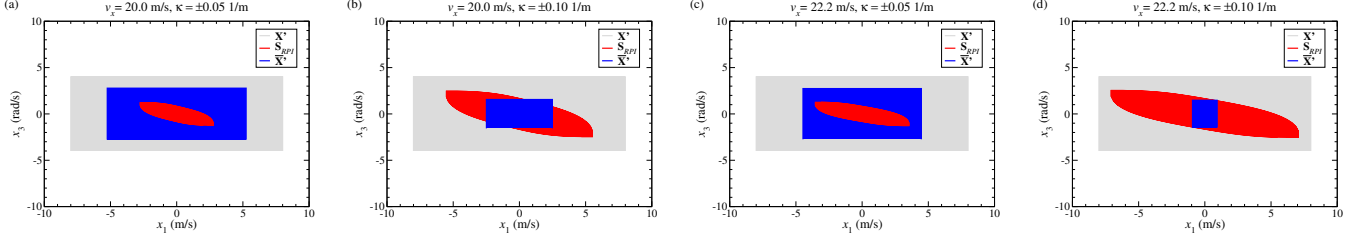


Fig. 1. Visualization of sets  $\mathbb{X}'$ ,  $\bar{\mathbb{X}}'$ , and  $\mathbb{S}_{RPI}$  when  $v_x = 20.0/22.2$  m/s and  $\kappa = \pm 0.05/\pm 0.1$  1/m. Here  $x_1 \equiv \dot{\Delta}$  and  $x_3 \equiv \dot{\theta}$ .

To enable real-time applications, (23) could be precomputed offline, and the results can be stored in a lookup table for online applications [8]. This table is denoted as the  $\kappa$ -table throughout this work. It outputs tightened constraints when  $\mathbb{X}'/\mathbb{U}'$ ,  $v_x$ , and  $\kappa$  are provided. Specifically, given  $\mathbb{X}'/\mathbb{U}'$  and  $v_x$ , the tightened constraints  $\bar{\mathbb{X}}'/\bar{\mathbb{U}}'$  corresponding to 201 data points for  $\kappa$  over the range  $[-0.1, 0.1]$  1/m with a uniform distribution are provided in the table. The tightened constraints needed for planning and control are derived online by looking up the nearest-neighbor state of the current input in the table. Fig. 1 presents typical results for a computation for the constraint region of actual system (gray), nominal system (blue), and disturbance invariant set (red) for  $v_x = 20.0/22.2$  m/s and  $\kappa = \pm 0.05/\pm 0.1$  1/m. The nominal constraint region  $\bar{\mathbb{X}}'$  decreases when the  $\mathbb{S}_{RPI}$  region increases. Consequently, the smallest set of feasible nominal states is obtained when  $v_x = 22.2$  m/s and  $\kappa = \pm 0.1$  1/m [Fig. 1(d)].

However, this method, which maps the currently detected  $\kappa$  to specified tightened constraints  $\bar{\mathbb{X}}'/\bar{\mathbb{U}}'$ , has two shortcomings. First, the input state does not precisely match the nearest-neighbor state in the table. Second, the fluctuations in the detected  $\kappa$  due to unknown external noise can result in constraint fluctuations, potentially leading to instability of the controlled system. As described in Sec. III-C, these problems are mitigated in this study by using the interpolation algorithm to compute improved tightened constraints.

#### IV. INTERPOLATION TUBE-CILQR ALGORITHM

This section details the proposed itube-CILQR algorithm. Convex and smooth exponential barrier functions are used to convert the constraints of Problem 3 into an equivalent unconstrained problem for the CILQR algorithm [14], [15]. The explicit form of the problem is as follows (Problem 4):

*Problem 4:*

$$\min_{\bar{\mathbf{x}}, \bar{\mathbf{u}}, \mathbf{L}} \bar{J}'_{int} = \bar{J}_s + \bar{J}_t + J_l + J_{x0} + J_{x1} + J_{x3} + J_u + J_{lu} + J_{ls}, \quad (24a)$$

$$\bar{J}_s = \sum_{i=0}^{N-1} \bar{\mathbf{x}}_i^T \mathbf{Q} \bar{\mathbf{x}}_i + \bar{\mathbf{u}}_i^T \mathbf{R} \bar{\mathbf{u}}_i, \quad (24b)$$

$$\bar{J}_t = \bar{\mathbf{x}}_N^T \mathbf{P} \bar{\mathbf{x}}_N, \quad (24c)$$

$$J_l = \sum_{i=0}^N \Lambda_i^T \mathbf{S} \Lambda_i, \quad (24d)$$

$$J_{x0} = q_{s1} \sum_{k=0,2}^N \exp \{ q_{s2} [\bar{x}_{k,\min} - \bar{x}_{k,i}] \} + \exp \{ q_{s2} [\bar{x}_{k,i} - \bar{x}_{k,\max}] \}, \quad (24e)$$

$$J_{x1} = \sum_{i=0}^N \exp \{ [ -(\lambda_{s,i} \bar{x}_{1,s} + \lambda_{d,i} \bar{x}_{1,det} + \lambda_{b,i} \bar{x}_{1,b}) - \bar{x}_{1,i} ] \} + \exp \{ [\bar{x}_{1,i} - (\lambda_{s,i} \bar{x}_{1,s} + \lambda_{d,i} \bar{x}_{1,det} + \lambda_{b,i} \bar{x}_{1,b})] \}, \quad (24f)$$

$$J_{x3} = \sum_{i=0}^N \exp \{ [ -(\lambda_{s,i} \bar{x}_{3,s} + \lambda_{d,i} \bar{x}_{3,det} + \lambda_{b,i} \bar{x}_{3,b}) - \bar{x}_{3,i} ] \} + \exp \{ [\bar{x}_{3,i} - (\lambda_{s,i} \bar{x}_{3,s} + \lambda_{d,i} \bar{x}_{3,det} + \lambda_{b,i} \bar{x}_{3,b})] \}, \quad (24g)$$

$$J_u = q_{u1} \sum_{i=0}^{N-1} \exp \{ q_{u2} [ -(\lambda_{s,i} \bar{\delta}_s + \lambda_{d,i} \bar{\delta}_{det} + \lambda_{b,i} \bar{\delta}_b) - \bar{\delta}_i ] \} + \exp \{ q_{u2} [\bar{\delta}_i - (\lambda_{s,i} \bar{\delta}_s + \lambda_{d,i} \bar{\delta}_{det} + \lambda_{b,i} \bar{\delta}_b)] \}, \quad (24h)$$

$$J_{lu} = q_{l1} \sum_{k=s,d,b}^N \sum_{i=0} \exp \{ q_{l2} [ -\lambda_{k,i} ] \} + \exp \{ q_{l2} [\lambda_{k,i} - 1.0] \}, \quad (24i)$$

$$J_{ls} = q_{l3} \sum_{i=0}^N \exp \{ q_{l4} [ 1.0 - (\lambda_{s,i} + \lambda_{d,i} + \lambda_{b,i}) ] \} + \exp \{ q_{l4} [ (\lambda_{s,i} + \lambda_{d,i} + \lambda_{b,i}) - 1.0 ] \} \quad (24j)$$

subject to

$$\bar{\mathbf{x}}_{i+1} = \bar{\mathbf{f}}(\bar{\mathbf{x}}_i, \bar{\mathbf{u}}_i), \quad 0 \leq i < N. \quad (25)$$

Here,  $\bar{x}_{1,det}$ ,  $\bar{x}_{3,det}$ , and  $\bar{\delta}_{det}$  are the upper bounds of the tightened constraints for  $\bar{x}_1$ ,  $\bar{x}_3$ , and  $\bar{\delta}$ , respectively; these parameters are derived by online lookup in the  $\kappa$ -table in accordance with the detected road curvature. The symbols  $\bar{x}_{1,s}/\bar{x}_{1,b}$ ,  $\bar{x}_{3,s}/\bar{x}_{3,b}$ , and  $\bar{\delta}_s/\bar{\delta}_b$  indicate the corresponding designed constraint bounds as described in Sec. III-C. The parameters  $\bar{x}_{0/2,min}$  and  $\bar{x}_{0/2,max}$  are the bounds of the original constraints of  $x_{0/2}$ . The scalars  $(q_{s1}, q_{s2})$ ,  $(q_{u1}, q_{u2})$ ,  $(q_{l1}, q_{l2})$ , and  $(q_{l3}, q_{l4})$  are the penalty parameters. The penalty parameters selected for this study are listed in Table II. In particular, the magnitude of  $\lambda_d$  was set to a constant of 0.5 to reduce the number of variables and thus decrease computational cost.

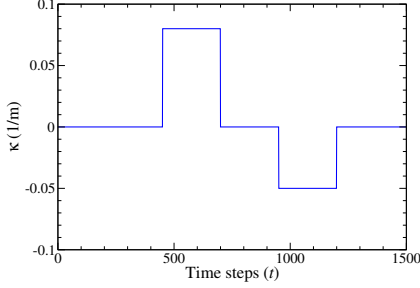


Fig. 2. Curvature profile for numerical simulations.

To solve Problem 4, the ILQR algorithm [16], [17] and Newton's descent method [25] were used to collaboratively optimize state, control, and interpolation variables iteratively through alternating backward and forward propagation steps. The relevant update laws for variables are then expressed as follows:

$$\hat{\mathbf{u}}_i = \bar{\mathbf{u}}_i + \tilde{\mathbf{k}}_i + \tilde{\mathbf{K}}_i (\hat{\mathbf{x}}_i - \bar{\mathbf{x}}_i), \quad (26a)$$

$$\hat{\mathbf{x}}_{i+1} = \bar{\mathbf{f}}(\hat{\mathbf{x}}_i, \hat{\mathbf{u}}_i), \quad (26b)$$

$$\hat{\Lambda}_i = \Lambda_i - [\mathbf{H}\bar{J}'_{int}(\Lambda_i)]^{-1} \nabla \bar{J}'_{int}(\Lambda_i). \quad (26c)$$

Here, the control gains  $\tilde{\mathbf{K}}_i$  and  $\tilde{\mathbf{k}}_i$  are computed using the analytical formulas presented in [16], [17]; the Hessian matrix  $\mathbf{H}\bar{J}'_{int}(\Lambda_i) \succ 0$ .

As described in previous sections, the control scheme used can be varied by varying the cost functions, input state  $\hat{\mathbf{x}}_0$ , and control input  $u$  to the actual system. These schemes are summarized as follows. i) itube-CILQR solves Problem 4 with the control action  $u$  of  $u_p$  (12), ii) tube-CILQR-up solves Problem 2 by CILQR with  $u_p$  (12), iii) tube-CILQR-un scheme solves Problem 2 by CILQR, with the control action  $u$  of  $u_n$  (10), iv) tube-CILQR-ua solves Problem 2 by CILQR, with the control action  $u_a$  (11), v) and nominal-CILQR solves Problem 1 by CILQR with the control law  $u_d$  (6). Problems 1–3 were also solved by using the Interior Point Optimizer (IPOPT) [26] software package for comparison with the results of the CILQR-based algorithms. These methods are denoted as MPC-based controllers in the following paragraphs and comprised itube-MPC, tube-MPC-up, tube-MPC-un, tube-MPC-ua, and nominal-MPC.

## V. EXPERIMENTAL RESULTS AND DISCUSSION

The proposed algorithm was evaluated against several other methods in numerical simulations and vision-based experiments in the TORCS environment. All experiments were conducted on a PC equipped with an Intel i9-9900K CPU, 64 GB of RAM, and an Nvidia RTX 2080 ti GPU with 11 GB of VRAM. The TORCS software provides sophisticated visualization and physics engines and accurately simulates both visual effects and vehicle dynamics for a self-driving vehicle and its surrounding environment [27], [28], [29]. Due to lag in the TORCS simulator, the actuation delay was approximately 6.66 ms on our computer for vision-based experiments; this lag was zero in numerical simulations.

### A. Numerical Simulations

This section presents numerical simulation results for the CILQR-based and MPC-based controllers. The test scenario was an ego-vehicle driving on a road with a cruising speed of 20.0 m/s. The road had several straight sections and two turns with constant curvatures  $\kappa = 0.08$  1/m (denoted as turn-1) and  $\kappa = -0.05$  1/m (denoted as turn-2), which are encountered at time steps  $450 \leq t \leq 700$  and  $950 \leq t \leq 1200$ , respectively (Fig. 2). The initial state of the ego-car was assumed to be at  $\mathbf{x}_0 = [2 \ 0 \ 0 \ 0]^T$ . We reiterate that  $x_0 \equiv \Delta$ ,  $x_1 \equiv \dot{\Delta}$ ,  $x_2 \equiv \theta$ ,  $x_3 \equiv \dot{\theta}$ , and  $u \equiv \delta$  throughout this work.

Fig. 3(a) presents the lateral offset ( $\Delta$ ) trajectories generated by the CILQR-based algorithms. This was the lateral position error of the ego-vehicle with respect to the lane centerline at each time step; it was a key indicator of performance in the lane-keeping task. These trajectories exhibited plateau curves at the curves of turn-1 and turn-2, indicating an offset of the output which is attributable to the constant nonzero road curvature. Similar behavior was observed in the trajectory-following results for a prototype autonomous four-wheel independent drive electric vehicle guided by an adaptive hierarchical control framework (Fig. 19 in [30]). As shown in Fig. 3(a), for various methods, the maximum lateral error occurred at turn-1 near  $t = 700$ . At this time step, the nominal-CILQR and tube-CILQR-ua control schemes had larger errors than the other schemes. Moreover, tube-CILQR-ua underperformed nominal-CILQR due to tightened constraints in the tube-based algorithm. This resulted in more conservative solution trajectories that deteriorated performance. However, the control law can be changed to overcome this problem; the tube-CILQR-un scheme, which uses the current nominal state as the controller input, was more accurate than nominal-CILQR and tube-CILQR-ua.

The lateral control performance of tube-CILQR-un can be further enhanced by two other approaches proposed. The tube-CILQR-up scheme uses the synthesized control law  $u_p = u_n + u_a$ ; this results in better performance than tube-CILQR-un or tube-CILQR-ua, which use  $u_n$  or  $u_a$  alone. The advantage of the tube-CILQR-up scheme is that the control laws  $u_n$  and  $u_a$  can collaboratively steer the  $\Delta$ -trajectory toward target zero points. However, this control strategy may generate nonsmooth control action trajectories when the control effort is high. As shown in Fig. 3(b), the steering angle ( $\delta$ ) curve obtained for tube-CILQR-up was not smooth at early time steps ( $t < 200$ ). By contrast, the corresponding  $\Delta$ -trajectory in Fig. 3(a) was stable at the same time interval. Second, the tracking performance of tube-CILQR-up scheme can be further improved by using the itube-CILQR algorithm. The itube-CILQR algorithm also uses the joint control law  $u_p$  and additionally applies interpolation to fuse multiple constraints [10]. This method can reduce system conservatism and enhance controller performance. As can be observed in the subplot of Fig. 3(a), the itube-CILQR algorithm had the lowest lateral error for turn-1 near  $t = 700$  of all of the tested CILQR-based methods.

Fig. 3(c) display the trajectories of the first element of the optimal interpolation variable sequences, namely  $\Lambda^* = [\lambda_b^* \ \lambda_d^* \ \lambda_s^*]^T$ . As described in Sec. IV, the magnitude of



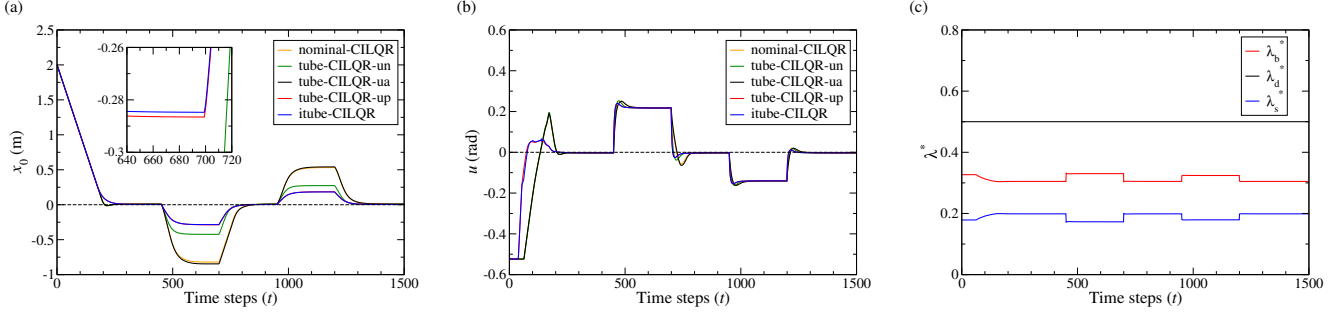


Fig. 3. Numerical simulation results for the CILQR algorithms obtained when  $v_x = 20.0$  m/s,  $|x_1| \leq 8.0$  m/s, and  $|x_3| \leq 4.0$  rad/s. (a) Trajectory of the actual system state  $x_0$ . (b) Trajectory of the actual system control input. (c) Trajectories of the first components of the optimal interpolation variable sequences for  $x_0 \equiv \Delta$  and  $u \equiv \delta$ . In (a) at  $t = 700$ ,  $x_0 = -0.2834$  and  $-0.2816$  m are the results of tube-CILQR-up and itube-CILQR, respectively. In (c),  $\Delta\lambda = 0.1453, 0.1060, 0.1574$ , and  $0.1449$  at  $t = 0, 300, 600$ , and  $1100$ , respectively.

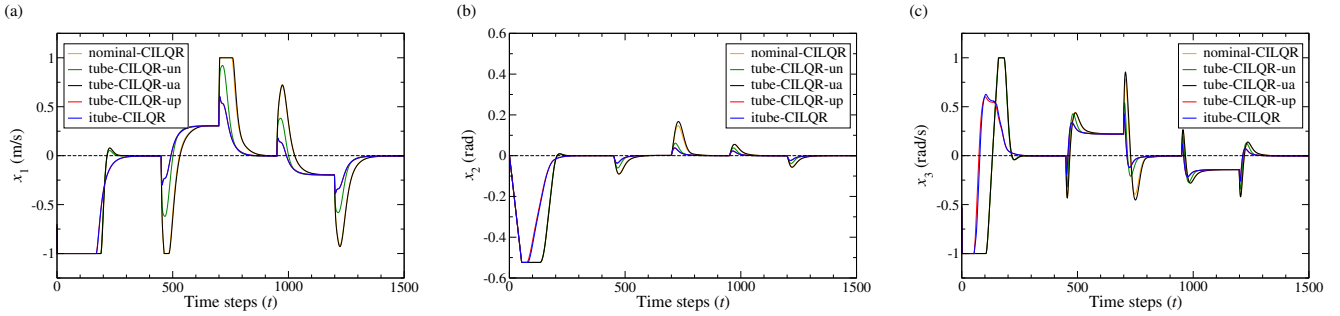


Fig. 4. Numerical simulation results for the CILQR algorithms derived for  $v_x = 20.0$  m/s,  $|x_1| \leq 8.0$  m/s, and  $|x_3| \leq 4.0$  rad/s. Trajectories of the actual system state (a)  $x_1$ , (b)  $x_2$ , and (c)  $x_3$ . Here,  $x_1 \equiv \dot{\Delta}$ ,  $x_2 \equiv \theta$ , and  $x_3 \equiv \dot{\theta}$ .

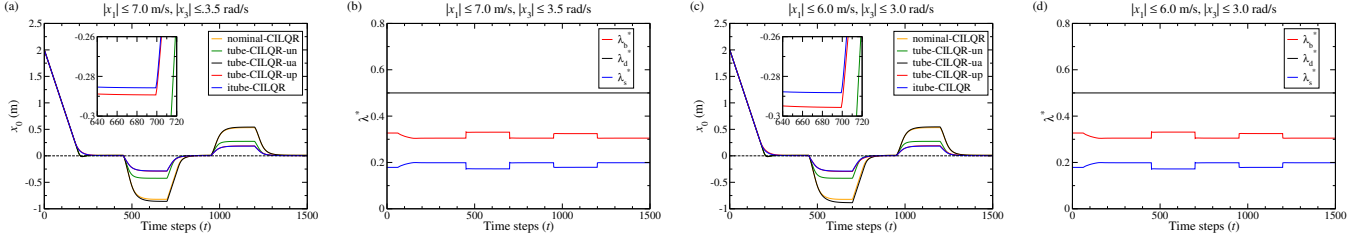


Fig. 5. Numerical simulation results for the CILQR algorithms derived for  $v_x = 20.0$  m/s. (a) and (b) were obtained with  $|x_1| \leq 7.0$  m/s, and  $|x_3| \leq 3.5$  rad/s. (c) and (d) were obtained with  $|x_1| \leq 6.0$  m/s, and  $|x_3| \leq 3.0$  rad/s. In (a) and (c) at the time step  $t = 700$ ,  $x_0 = -0.2862$  and  $-0.2826$  m were obtained by tube-CILQR-up and itube-CILQR, respectively. In (b),  $\Delta\lambda = 0.1454, 0.1061, 0.1581$ , and  $0.1452$  at  $t = 0, 300, 600$ , and  $1100$ , respectively. In (d),  $\Delta\lambda = 0.1454, 0.1062, 0.1590$ , and  $0.1458$  at  $t = 0, 300, 600$ , and  $1100$ , respectively.

$\lambda_d^*$  is set to a constant value of 0.5 for reducing computational effort. We measured the conservatism of the system as the difference between  $\lambda_b^*$  and  $\lambda_s^*$  as follows:

$$\Delta\lambda \equiv \lambda_b^* - \lambda_s^*. \quad (27)$$

Overall,  $\Delta\lambda > 0$  held during the whole maneuver, indicating that the less conservative system had a lower cost. Conservatism could be further reduced at the curves;  $\Delta\lambda$  increased as the road curvature increases. Moreover, the difference was larger at the curvier section (turn-1) than at the less-curved section (turn-2), indicating that the trajectories of the interpolation variables can adaptively respond to disturbance. A similar

adaptive response behavior was also observed in our previous work [25] for slack variables, which were incorporated into a CILQR algorithm with a similar role to the interpolation variables in this study. Therefore, this behavior of the  $\lambda^*$ -trajectories may be the reason that itube-CILQR outperformed tube-CILQR-up in the  $\Delta$ -trajectories as indicated in Fig. 3(a). Figs. 4(a), 4(b), and 4(c) present the  $\dot{\Delta}$ ,  $\theta$ , and  $\dot{\theta}$  trajectories, respectively. The minimum value of  $\theta$  is truncated at early time steps ( $t < 150$ ) because  $\delta^*$ -trajectories in Fig. 3(b) are constrained to the range  $[-\pi/6, \pi/6]$  to prevent the steering input from exceeding physical limitations. The  $\dot{\Delta}$  and  $\dot{\theta}$  values in Fig. 4(a) and 4(c) were further clipped to the interval  $[-1.0,$



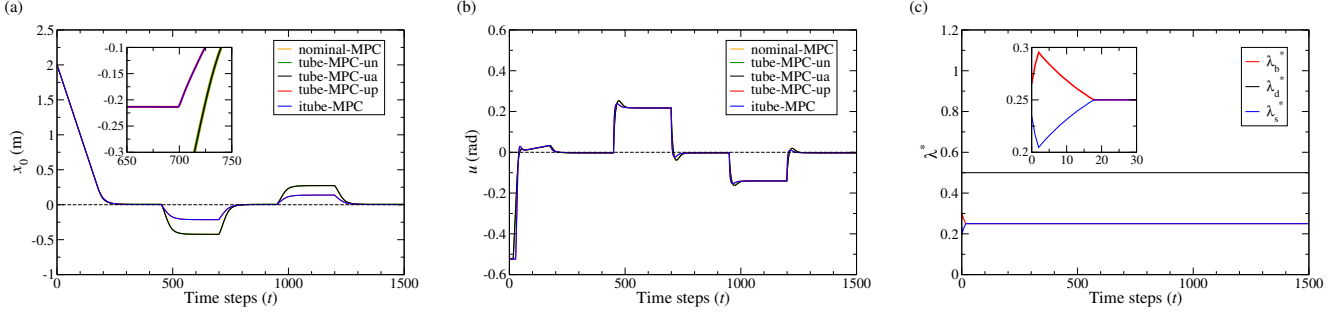


Fig. 6. Numerical simulation results of the MPC algorithms for  $v_x = 20.0$  m/s,  $|x_1| \leq 8.0$  m/s, and  $|x_3| \leq 4.0$  rad/s. (a) Trajectory of the actual system state  $x_0$ . (b) Trajectory of the actual system control input. (c) Trajectories of the first components of the optimal interpolation variable sequences. In (a),  $x_0 = -0.2104$  m at  $t = 700$  was obtained for both tube-MPC-up and for itube-MPC.

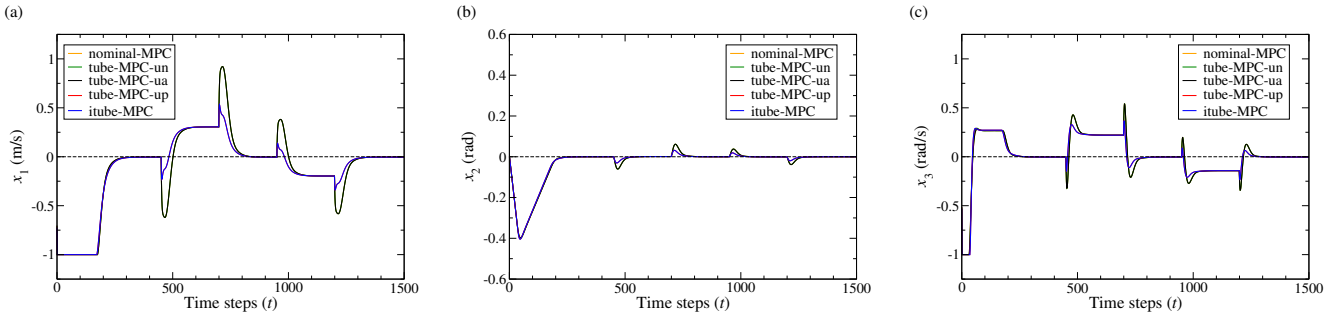


Fig. 7. Numerical simulation results for the MPC algorithms obtained when  $v_x = 20.0$  m/s,  $|x_1| \leq 8.0$  m/s, and  $|x_3| \leq 4.0$  rad/s. Trajectories of the actual system state for (a)  $x_1$ , (b)  $x_2$ , and (c)  $x_3$ .

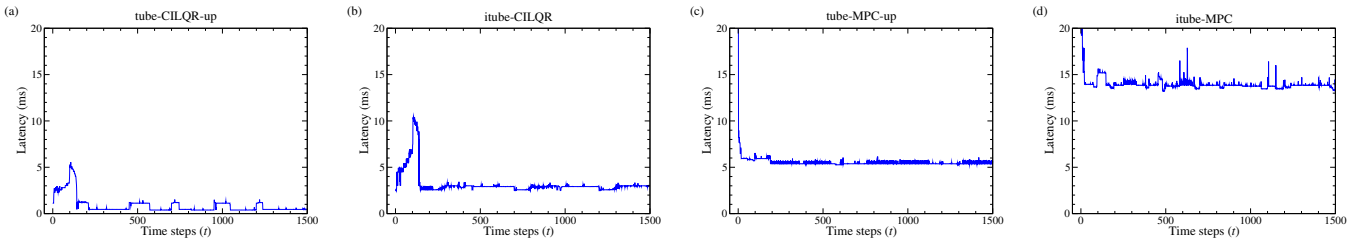


Fig. 8. Computation time of (a) tube-CILQR-up, (b) itube-CILQR, (c) tube-MPC-up, and (d) itube-MPC algorithms at each time step.

1.0] to ensure comfort for vehicle occupants.

Fig. 5 presents the lane-keeping results for the algorithms when using smaller constraint regions. The  $\Delta$ -trajectories in Fig. 3(a), Fig. 5(a), and Fig. 5(c) reveal that the tracking performance improved (the lateral error decreased) when the system conservatism was reduced by increasing the constraint region. Consequently, at turn-1, itube-CILQR had the smallest lateral error when  $|x_1| \leq 8.0$  m/s and  $|x_3| \leq 4.0$  rad/s [Fig. 3(a)]; it had a larger lateral error when  $|x_1| \leq 7.0$  m/s and  $|x_3| \leq 3.5$  rad/s [Fig. 5(a)] or when  $|x_1| \leq 6.0$  m/s and  $|x_3| \leq 3.0$  rad/s [Fig. 5(c)]. The  $\lambda^*$ -trajectories in Fig. 3(c), Fig. 5(b), and Fig. 5(d) indicate that the gap  $\Delta\lambda$  generally increased when the constraint region decreased; this trend was also observed for the difference in the lateral errors generated by itube-CILQR and tube-CILQR-up for turn-1. Near  $t = 700$ , the largest lateral error difference was when  $|x_1| \leq 6.0$  m/s

and  $|x_3| \leq 3.0$  rad/s [Fig. 5(c)].

Trajectories generated by the MPC-based controllers are shown in Figs. 6 and 7 for comparison against those of the CILQR-based controllers. In general,  $\Delta$ -trajectories produced by MPC-based algorithms have smaller lateral error than those of CILQR-based algorithms [Fig. 6(a)]. This may have occurred because the MPC-based schemes use the primal-dual-based IPOPT solver, whereas CILQR-based schemes are simply primal-based optimization methods. The  $\Delta$ -trajectories obtained by the IPOPT solver can be classified into two groups in Fig. 6(a): those of nominal-MPC, tube-MPC-un, and tube-MPC-ua algorithms and those of tube-MPC-up and itube-MPC algorithms. The tube-MPC-up and itube-MPC schemes had smaller lateral error than the other methods. Nevertheless, the behavior of the  $\Delta$ -trajectories obtained by tube-MPC-up and itube-MPC were similar, as indicated in the curves in the

TABLE III  
AVERAGE COMPUTATION TIME FOR THE TUBE-CILQR-UP, ITUBE-CILQR, TUBE-MPC-UP, AND ITUBE-MPC ALGORITHMS

Method	tube-CILQR-up	itube-CILQR	tube-MPC-up	itube-MPC
Latency (ms)	0.87	3.16	5.54	14.75

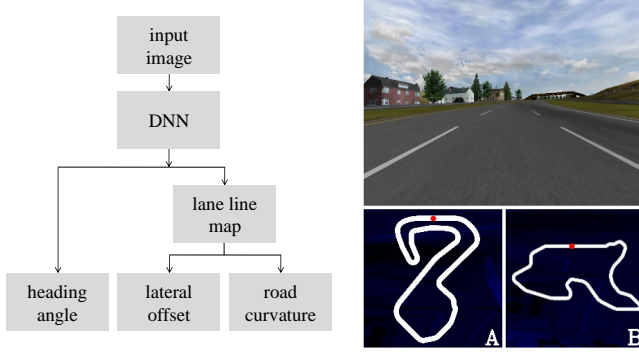


Fig. 9. Illustration of the vision perception system (left), and an example traffic scene and maps of track-A and track-B in TORCS for autonomous driving (right). The input to the DNN was an RGB image with resolution  $228 \times 228$  pixels. The ego-car was designed to begin maneuvering at the locations marked by red symbols on the track maps. The driving direction was counterclockwise.

subfigure in Fig. 6(a); they were not split as in the tube-CILQR-up scheme [Fig. 3(a)] even for the smaller constraint region of  $|x_1| \leq 5.6$  m/s and  $|x_3| \leq 2.5$  rad/s (not shown in the figures). Fig. 6(c) displays the  $\lambda^*$ -trajectories derived by the itube-MPC scheme. Compared with the trajectories of itube-CILQR algorithm [Fig. 3(c)], itube-MPC initially had lower conservatism (at  $t < 20$ ) when gap  $\Delta\lambda > 0$ . Subsequently, the gap  $\Delta\lambda$  converged to zero, even on curves. This may explain why the  $\Delta$ -trajectories produced by itube-MPC and tube-MPC-up algorithms in Fig. 6(a) are the same on turn-1 and turn-2. Because the IPOPT solver likely produces nearly optimal solutions for both itube-MPC or tube-MPC-up, the same results are obtained for both schemes.

The computational time required to obtain a trajectory for tube-CILQR-up, itube-CILQR, tube-MPC-up, and itube-MPC controllers are presented in Fig. 8(a), 8(b), 8(c), and 8(d), respectively. At early time steps ( $t < 200$ ), the tube-CILQR-up and itube-CILQR algorithms require up to 5 and 10 ms, respectively, to generate a solution. By contrast, the MPC-based algorithms using the IPOPT software package required longer ( $>20$  ms) to find solutions because finding an appropriate starting points for optimization is difficult in IPOPT due to its reliance on the interior-point method [26]. On average, the tube-MPC-up and itube-MPC algorithms required approximately 1.75 and 4.67 times longer, respectively, to yield control commands compared with itube-CILQR (Table III). Therefore, a clear trade-off between the itube-CILQR and itube-MPC algorithms in terms of computational burden and performance can be observed. Compared with itube-MPC algorithm, itube-CILQR had a lower computational cost. Moreover, it maintained satisfactory performance with a lateral error of less than 0.3 m on turn-1 [Figs. 3(a) and 6(a)]. In accordance with these findings, the proposed itube-CILQR

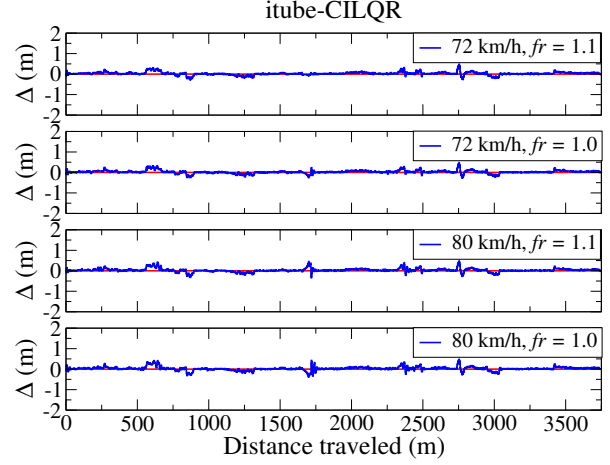


Fig. 10. Trajectories obtained for  $\Delta$  by using the itube-CILQR controller under  $fr = 1.1$  or  $1.0$  for an ego-vehicle traveling on track-A at 72 or 80 km/h.

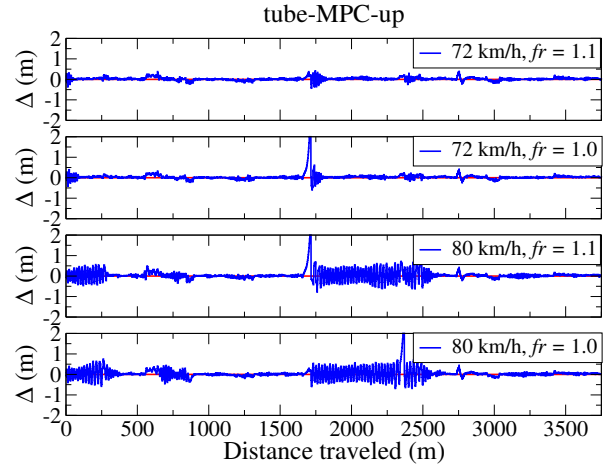


Fig. 11. Trajectories obtained for  $\Delta$  by using the tube-MPC-up controller under  $fr = 1.1$  or  $1.0$  for an ego-vehicle traveling on track-A at 72 or 80 km/h.

algorithm with the parameter setting in Figs. 3 and 4 was compared with its counterparts, the tube-MPC-up and itube-MPC algorithms, for vision-based maneuvers. The results are in the following section.

### B. Vision-guided Lane-Keeping Experiments

Vehicle lane-keeping control is a key function of autonomous vehicles, and computer-vision-based approaches

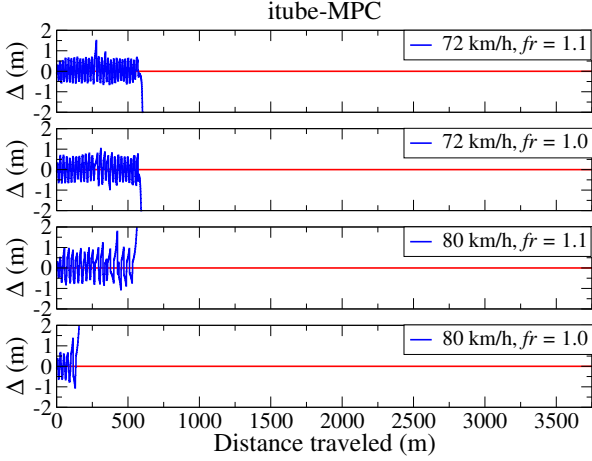


Fig. 12. Trajectories obtained for  $\Delta$  by using the itube-MPC controller under  $fr = 1.1$  or  $1.0$  for an ego-vehicle traveling on track-A at 72 or 80 km/h.

TABLE IV  
AVERAGE  $\Delta\lambda$  VALUES DURING LANE-KEEPING MANEUVERS USING THE ITUBE-CILQR CONTROLLER

$fr$	track-A		track-B	
	80 km/h	72 km/h	80 km/h	72 km/h
0.80	0.115080	0.113438	0.112595	0.111686
0.85	0.113745	0.113639	0.112104	0.111734
0.90	0.114120	0.113503	0.112282	0.111570
1.00	0.114457	0.113747	0.112355	0.111741
1.10	0.114544	0.114034	0.112223	0.111784
Average	0.114389	0.113672	0.112311	0.111703

have been studied by many researchers [19], [20], [31]. A vision system developed in our previous work [21] that uses a deep neural network (DNN) to extract image features was used to maneuver the ego-vehicle in the TORCS environment in conjunction with control algorithms. The DNN used in the visual perception module could output data for autonomous driving at a speed of 40 frames per second (Fig. 9). It generated the ego-vehicle heading angle  $\theta$  and a binary lane line map simultaneously by using a multitask UNet [32]. The lateral offset  $\Delta$  and road curvature  $\kappa$  were then derived using postprocessing methods [21]. Here,  $\theta$ ,  $\Delta$ , and  $\kappa$  were obtained with respect to the current position of the ego-car. Subsequently, the itube-CILQR, tube-MPC-up, and itube-MPC controllers were used to guide the ego-car to track the lane centerline in TORCS. The tube-MPC-up controller was operated with tightened constraints, which were looked up directly from the  $\kappa$ -table described in Sec. III-D. For the itube-CILQR or itube-MPC schemes, the tightened constraints from the  $\kappa$ -table were used to compute improved tightened constraints following the procedure described in Sec. III-C. The testing environments track-A and track-B were both three-lane highways with a lane width of 4 m. Respectively, their total lengths were 3919 and 4441 m, and their maximum curvatures were approximately 0.05 and 0.03 1/m. Variational road friction (denoted as  $fr$ ) was also applied in the TORCS environment in the range [0.8,

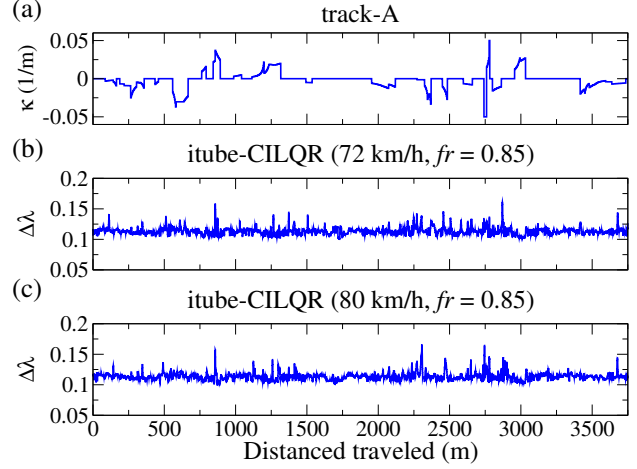


Fig. 13. Comparisons of lane curvature  $\kappa$  and computed gap  $\Delta\lambda$ . (a) Curvature profile of track-A. Trajectories obtained for  $\Delta\lambda$  by using the itube-CILQR controller under  $fr = 0.85$  for an ego-vehicle traveling at (b) 72 and (c) 80 km/h. The results of the associated quantitative analyses are presented in Table IV.

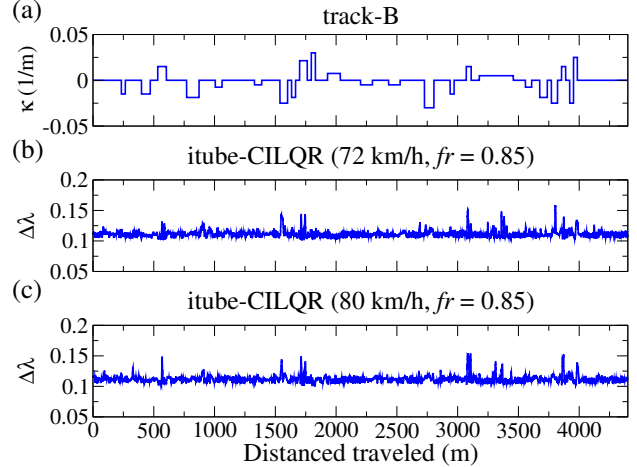


Fig. 14. Comparisons of lane curvature  $\kappa$  and computed gap  $\Delta\lambda$ . (a) Curvature profile of track-B. Trajectories obtained for  $\Delta\lambda$  by using the itube-CILQR controller under  $fr = 0.85$  for an ego-vehicle traveling at (b) 72 and (c) 80 km/h. The results of the associated quantitative analyses are presented in Table IV.

1.1] to test the algorithm's performance [33]. The DNN was trained on track-B data but not on track-A data to emulate unsupervised and supervised training scenarios. In both cases, vehicle maneuvering was successful [34]. In addition to lateral CILQR or MPC controllers, the ego-vehicle was also controlled by a proportional-integral controller [21] to maintain a constant longitudinal speed of 72 or 80 km/h (20.0 or 22.2 m/s) during lane-keeping maneuvers.

Figs. 10 and 11 present the  $\Delta$ -trajectories of ego-vehicle guided by the itube-CILQR and tube-MPC-up controllers at a cruising speed of 72 or 80 km/h on track-A when  $fr = 1.0$  or  $1.1$ . Both controllers could maneuver the ego-vehicle,

which accomplished the lane-keeping task over a full lap on track-A. The ego-vehicle controlled by the proposed itube-CILQR controller was more frequently at the lane center (lower lateral error) than the vehicle controlled by the tube-MPC-up controller. The itube-CILQR controller had a lateral error of less than 0.5 m for all cases. However, the  $\Delta$ -trajectories received for the tube-MPC-up controller oscillated substantially, resulting in a larger average lateral error than that of itube-CILQR. This behavior resulted from steering lag, which was caused by finite controller latency [35]. As shown in Fig. 8(b), the latency of itube-CILQR algorithm was shorter than the actuation delay (6.66 ms) of the ego-vehicle in TORCS, whereas the tube-MPC-up algorithm latency generally met or exceeded this delay [Fig. 8(c)]. Fig. 12. presents the lane-keeping results for itube-MPC. Due to the long controller latency of the itube-MPC algorithm [Fig. 8(d)], the trajectories had more severe oscillation than those for tube-MPC-up. Thus, ego-vehicle controlled by itube-MPC left the lane unintentionally. In the worst case, itube-MPC failed to maintain the ego-car in the lane at approximately 160 m for a speed of 80 km/h and  $fr = 1.0$ . In summary, the itube-CILQR algorithm outperformed tube-MPC-up and itube-MPC in vision-guided lane-keeping maneuvers, primarily due to its faster rapid computation speed.

Figs. 13 and 14 present comparisons of the curvature profiles and  $\Delta\lambda$ -trajectories obtained by using itube-CILQR algorithm on track-A and track-B, respectively, under various conditions. In general, the data points of the  $\Delta\lambda$ -trajectories were greater than zero on both track, indicting that itube-CILQR was less conservative than standard tube-based approaches. The peaks in the  $\Delta\lambda$ -trajectories indicated predicted cornering cases for which greater curvature was detected. These results were generally similar to those in the numerical simulations [Fig. 3(c), Fig. 5(b), and Fig. 5(d)]. The results derived on unsupervised track-A were qualitatively noisy [Fig. 13(b) and Fig. 13(c)]; this could be attributable to several factors, such as the irregular curvature profile, algorithm latency, insufficient detection range of the lane detector [19], unstable and inconsistent lane inference results [20], or low lane marker quality [31]. These factors are general problems that could decrease safety for autonomous vehicles using lane detection results. By contrast, maneuvers performed on supervised track-B resulted in fewer distinct peaks in  $\Delta\lambda$ -trajectories than in trajectories for track-A [Fig. 14(b) and Fig. 14(c)]. The corresponding quantitative analyses are provided in Table IV; the average value of  $\Delta\lambda$  was lower for track-B than for track-A. This indicates that vehicle maneuvering is superior for roads used for training (track-B in this case) with the same DNN architecture. Thus, training on the target road is a straightforward approach for improving algorithm performance and thereby enhancing autonomous driving safety.

## VI. CONCLUSIONS

This paper proposes a novel itube-CILQR algorithm based on the CILQR optimizer [14], [15] and an interpolation tube-based MPC approach [10]. The optimizer has high computation speed, and, in the tube-based method, improved tightened

constraints were computed using varying disturbance bounds. In addition, a synthesized control law [11] was used for the robust control of the actual system. The disturbance considered in this study resulted from road curvature, which could be detected online along with the ego-vehicle heading angle and lateral offset during a lane-keeping task by using a visual perception system [21]. The effectiveness of itube-CILQR algorithm was validated through numerical and vision-based experiments conducted on large-curvature roads with variational road friction in TORCS. The itube-CILQR algorithm had satisfactory performance in numerical simulations and further outperformed itube-MPC algorithm implemented using the IPOPT solver in real-time vision-based maneuvers. The itube-CILQR algorithm had a fast average computation time of approximately 3.16 ms in these experiments, whereas the average latency of itube-MPC algorithm was longer than 14.75 ms. Moreover, the itube-CILQR algorithm reduced conservatism, thereby enhancing system performance compared with control by standard tube-based approaches, such as tube-CILQR-up. The features of itube-CILQR algorithm, including real-time performance, guaranteed robustness, and lower conservatism, indicate its excellent potential for robust automotive control not only in academic research but also in practical applications.

## REFERENCES

- [1] J. B. Rawlings, "Tutorial overview of model predictive control," *IEEE Control Systems Magazine*, vol. 20, no. 3, pp. 38–52, June 2000.
- [2] S. V. Raković, S. Zhang, H. Sun and Y. Xia, "Model Predictive Control for Linear Systems Under Relaxed Constraints," *IEEE Trans. Autom. Control*, vol. 68, no. 1, pp. 369–376, Jan 2023.
- [3] J. B. Rawlings, D. Q. Mayne, and M. M. Diehl, *Model Predictive Control: Theory, Computation, and Design*. Nob Hill Publishing, 2017.
- [4] Y. Gao, A. Gray, H. E. Tseng and F. Borrelli, "A tube-based robust nonlinear predictive control approach to semiautonomous ground vehicles," *Vehicle System Dynamics*, vol. 52, no. 6, pp. 802–823, 2014.
- [5] S. Mata, A. Zubizarreta and C. Pinto, "Robust Tube-Based Model Predictive Control for Lateral Path Tracking," *IEEE Trans. Intell. Veh.*, vol. 4, no. 4, pp. 569–577, Dec 2019.
- [6] S. Khaitan, Q. Lin and J. M. Dolan, "Safe Planning and Control Under Uncertainty for Self-Driving," *IEEE Trans. Veh. Technol.*, vol. 70, no. 10, pp. 9826–9837, 2021.
- [7] W. Wang, Y. Zhang, C. Yang, T. Qie and M. Ma, "Adaptive Model Predictive Control-Based Path Following Control for Four-Wheel Independent Drive Automated Vehicles," *IEEE Trans. Intell. Transp. Syst.*, vol. 23, no. 9, pp. 14399–14412, 2022.
- [8] H. Yong, S. Lu, W. Xie, T. Cui and F. Yang, "Autonomous Vehicle Path Tracking: Stochastic Tube Model Predictive Control with Covariance Steering and Discounted Chance Constraints," *IEEE Trans. Veh. Technol.*, doi: 10.1109/TVT.2024.3522673.
- [9] R. González, M. Fiacchini, J. L. Guzmán, T. Álamo and F. Rodríguez, "Robust tube-based predictive control for mobile robots in off-road conditions," *Robotics and Autonomous Systems*, vol. 59, no. 10, pp. 711–726, 2011.
- [10] M. Kögel and R. Findeisen, "Fusing multiple time varying tubes for robust MPC," *IFAC-PapersOnLine*, 53(2), pp. 7055–7062, 2020.
- [11] D. Q. Mayne, E. C. Kerrigan, and P. Falugi, "Robust model predictive control: advantages and disadvantages of tube-based methods," *IFAC Proceedings Volumes*, 44(1), 191–196, 2011.
- [12] G. Williams, B. Goldfain, P. Drews, K. Saigol, J. Rehg, E. Theodorou, "Robust Sampling Based Model Predictive Control with Sparse Objective Information," in *Proceedings of Robotics: Science and Systems*, 2018.
- [13] R. Andrade, J. E. Normey-Rico, and G. V. Raffo, "Fast embedded tube-based MPC with scaled-symmetric ADMM for high-order systems: Application to load transportation tasks with UAVs," *ISA Transactions*, vol. 156, pp. 70–86, 2025.
- [14] J. Chen, W. Zhan and M. Tomizuka, "Autonomous Driving Motion Planning With Constrained Iterative LQR," *IEEE Trans. Intell. Veh.*, vol. 4, no. 2, pp. 244–254, June 2019.

- [15] Y. Liu, X. Pei, H. Zhou and X. Guo, "Spatiotemporal Trajectory Planning for Autonomous Vehicle Based on Reachable Set and Iterative LQR," *IEEE Trans. Veh. Technol.*, vol. 73, no. 8, pp. 10932-10947, Aug. 2024.
- [16] Y. Tassa, T. Erez and E. Todorov, "Synthesis and stabilization of complex behaviors through online trajectory optimization," in *IEEE/RSJ International Conference on Intelligent Robots and Systems*, 2012, pp. 4906-4913.
- [17] Y. Tassa, N. Mansard and E. Todorov, "Control-limited differential dynamic programming," in *IEEE International Conference on Robotics and Automation (ICRA)*, 2014, pp. 1168-1175.
- [18] R. Rajamani, *Vehicle Dynamics and Control*. Springer, 2011.
- [19] S. Xu, H. Peng, P. Lu, M. Zhu and Y. Tang, "Design and Experiments of Safeguard Protected Preview Lane Keeping Control for Autonomous Vehicles," *IEEE Access*, vol. 8, pp. 29944-29953, 2020.
- [20] T. Getahun and A. Karimoddini, "An Integrated Vision-Based Perception and Control for Lane Keeping of Autonomous Vehicles," *IEEE Trans. Intell. Transp. Syst.*, vol. 25, no. 8, pp. 9001-9015, Aug. 2024.
- [21] D.-H. Lee, "Efficient Perception, Planning, and Control Algorithm for Vision-Based Automated Vehicles," *Appl. Intell.* vol. 54, pp. 8278-8295, 2024.
- [22] B. Wymann, "TORCS: The Open Racing Car Simulator." <https://sourceforge.net/projects/torcs/>
- [23] K. Lee, S. Jeon, H. Kim and D. Kum, "Optimal Path Tracking Control of Autonomous Vehicle: Adaptive Full-State Linear Quadratic Gaussian (LQG) Control," *IEEE Access*, vol. 7, pp. 109120-109133, 2019.
- [24] L. Güvenç, B. Aksun-Güvenç, S. Zhu, Ş. Y. Gelbal, *Autonomous Road Vehicle Path Planning and Tracking Control*. IEEE Press, 2022.
- [25] D.-H. Lee, "Lane-Keeping Control of Autonomous Vehicles Through a Soft-Constrained Iterative LQR", 2023, *arXiv:2311.16900*. [Online]. Available: <https://arxiv.org/abs/2311.16900>
- [26] A. Wächter and L. T. Biegler, "On the implementation of an interior-point filter line-search algorithm for large-scale nonlinear programming," *Math. Program.*, vol. 106, no. 1, pp. 25-57, May 2006.
- [27] C. Chen, A. Seff, A. Kornhauser, and J. Xiao, "DeepDriving: Learning affordance for direct perception in autonomous driving," in *Proceedings of the IEEE International Conference on Computer Vision*, 2015, pp. 2722-2730.
- [28] L. Cardamone, P. L. Lanzi and D. Loiacono, "TrackGen: An interactive track generator for TORCS and Speed-Dreams," *Applied Soft Computing*, vol. 28, pp. 550-558, 2015.
- [29] D.-H. Lee, K.-L. Chen, K.-H. Liou, C.-L. Liu, and J.-L. Liu, "Deep learning and control algorithms of direct perception for autonomous driving," *Appl. Intell.* vol. 51, pp. 237-247, 2021.
- [30] J. Guo, Y. Luo and K. Li, "An Adaptive Hierarchical Trajectory Following Control Approach of Autonomous Four-Wheel Independent Drive Electric Vehicles," *IEEE Trans. Intell. Transp. Syst.*, vol. 19, no. 8, pp. 2482-2492, Aug. 2018.
- [31] J. H. Yang, W. Y. Choi and C. C. Chung, "StrikeNet: Deep Convolutional LSTM-Based Road Lane Reconstruction With Spatiotemporal Inference for Lane Keeping Control," *IEEE Access*, vol. 12, pp. 97500-97514, Sept 2024.
- [32] O. Ronneberger, P. Fischer, and T. Brox, "U-Net: Convolutional networks for biomedical image segmentation," in *International Conference on Medical Image Computing and Computer-Assisted Intervention (MICCAI)*, Springer, 2015, pp. 234-241.
- [33] M. R. Bonyadi, Z. Michalewicz, S. Nallaperuma and F. Neumann, "Ahura: A Heuristic-Based Racer for the Open Racing Car Simulator," *IEEE Transactions on Computational Intelligence and AI in Games*, vol. 9, no. 3, pp. 290-304, Sept. 2017.
- [34] Y. Wu, S. Liao, X. Liu, Z. Li and R. Lu, "Deep Reinforcement Learning on Autonomous Driving Policy With Auxiliary Critic Network," *IEEE Trans. Neural Netw. Learn. Syst.*, vol. 34, no. 7, pp. 3680-3690, July 2023.
- [35] S. Xu, H. Peng and Y. Tang, "Preview Path Tracking Control With Delay Compensation for Autonomous Vehicles," *IEEE Trans. Intell. Transp. Syst.*, vol. 22, no. 5, pp. 2979-2989, May 2021.